HiSST: 3rd International Conference on
High-Speed Vehicle Science & Technology
14–19 April 2024, Busan, Korea

# Verification of nonequilibrium chemistry model for hypersonic computational fluid dynamics against first-principles molecular-dynamics simulations

*Erik Torres*[1], *Thomas E. Schwartzentruber*[2]

## Abstract

We perform verification studies of the Modified Marrone-Treanor multi-temperature nonequilibrium chemistry model for computational fluid dynamics on several canonical flow fields. Reference solutions suitable for testing the model in scenarios applicable to hypersonic flight and ground test facilities have been generated via first-principles Direct Molecular Simulations. This molecular-scale simulation method relies exclusively on ab initio potential energy surfaces generated by computational chemists to predict the chemical and thermodynamic evolution of the flow field. The Modified Marrone-Treanor model for CFD has been built upon a consistent foundation by employing kinetic rates and vibrational energy-chemistry coupling terms derived from the same potential energy surfaces.

**Keywords:** *Thermo-chemical nonequilibrium, computational fluid dynamics, ab initio potentials, direct molecular simulation*

## 1. Introduction

Over the last decade more than 20 ab initio potential energy surfaces (PESs) suitable for studying the major gas-phase reactions in shock-heated air from first principles have been released by the Computational Chemistry group at the University of Minnesota. These PESs provide the forces on arbitrary spatial arrangements of 3-4 atomic nuclei representing the constituents of the major air species ($N_2$, $O_2$, NO, N and O) during a collision. They have been employed by our group and other researchers in two main ways:

1. As part of quasi-classical trajectory (QCT) calculations [1] to generate reaction rate data for the major reactions (oxygen and nitrogen dissociation and the Zeldovich exchange reactions responsible for producing nitric oxide behind strong shocks). Kinetic databases generated in this manner are subsequently employed in nonequilibrium finite-rate-chemistry models for computational fluid dynamics (CFD). The Modified Marrone-Treanor (MMT) model [2] makes use of these first-principles-derived dissociation rate data for $N_2$ and $O_2$ and has been implemented in US3D [3], the high-performance hypersonic CFD code developed at the University of Minnesota. It naturally accounts for vibrational bias in dissociation rates and average vibrational energy removed by dissociation. More recently, the model's kinetic database has been extended with new QCT-derived mixed dissociation and exchange reactions [4]. This makes full-scale hypersonic flow simulations involving high-temperature air chemistry based only on first-principles rate data possible.
2. Embedded in a classical-trajectory direct simulation Monte Carlo algorithm, also known as Direct Molecular Simulation (DMS) [5]. In this configuration the PESs are responsible for shaping the entire flow field, by determining the outcome of individual collisions being simulated on-the-fly as part of a particle-based dilute-gas kinetic simulation scheme. This approach has been used to generate reference solutions in space-homogeneous (0D) reactors [4] and more complex 1D [6] and

[1] *Researcher, Department of Aerospace Engineering and Mechanics, University of Minnesota, USA, etorres@umn.edu*
[2] *Professor, Department of Aerospace Engineering and Mechanics, University of Minnesota, USA, schwart@umn.edu*

2D flow fields [7, 8]. Such solutions are computationally costly, but uniquely suited for verification of the aforementioned chemistry models employed in fluid-dynamics simulations.

In Secs. 2-4 we discuss three recent verification studies to test the Modified Marrone-Treanor (MMT) model's performance under a variety of conditions. We compare CFD results for chemically reacting flows obtained with the MMT model against benchmark solutions (generated by ourselves and others) via the first-principles Direct Molecular Simulation method.

## 2. Normal shock in air

Our most recent additions to the 5-species air kinetic database for use with the MMT model have been verified against space-homogeneous (0D) heat bath cases under isothermal and adiabatic conditions [9, 10]. Currently we are in the process of extending these verification studies to one-dimensional, unsteady flow. Our test case consists of a normal shock wave in air at a nominal speed of $6\,\mathrm{km/s}$. We simulate the normal shock problem by feeding in a supersonic stream of cold air at the left boundary of a 1D domain and stagnating the flow at a symmetry boundary at the other end. This produces a shock wave traveling back upstream (right-to-left), compressing the gas behind it, heating it to become vibrationally excited and to partially dissociate. Once atomic oxygen and nitrogen appear in the flow, exchange reactions with collision partners $N_2$ and $O_2$ produce nitric oxide.

We carry out the DMS benchmark calculation of this 1D shock wave using the same approach that was originally outlined in Ref. [6] for an $O_2/O$ mixture. For the present 5-species air mixture and a steady-state shock speed of $6\,\mathrm{km/s}$, the pre- and post-shock equilibrium conditions are summarized in Table 1.

**Table 1.** Pre- and post-shock equilibrium conditions for 5-species air at shock speed $6\,\mathrm{km/s}$. (ground-electronic-state contributions to thermodynamic properties only). Mixture composition specified in terms of mole fractions $x_i$.

| | | (1) upstream | (2) downstream |
|---|---|---|---|
| $u$ | [m/s] | 6000 | 411.8 |
| $p$ | [Pa] | 15.00 | 5824 |
| $T$ | [K] | 300.0 | 5605 |
| $x_{N_2}$ | | 0.8000 | 0.4000 |
| $x_{O_2}$ | | 0.2000 | 0.0000 |
| $x_{NO}$ | | 0.0000 | 0.0019 |
| $x_{N}$ | | 0.0000 | 0.3196 |
| $x_{O}$ | | 0.0000 | 0.2785 |
| $\rho \times 10^3$ | [kg/m$^3$] | 0.1733 | 2.524 |
| $h$ | [MJ/kg] | 0.00 | 17.92 |
| $\frac{1}{2}u^2$ | [MJ/kg] | 18.00 | 0.08 |
| $h_0$ | [MJ/kg] | 18.00 | |

As discussed in Ref. [6], the steady-state problem in the shock's frame of reference is actually simulated as an unsteady problem in the frame attached to the post-shock equilibrium gas. This requires one to adjust the inflow velocity of the cold upstream from Table 1 accordingly, i.e. $u_1' = u_1 - u_2$. The DMS code used to generate the benchmark solution for the present test case is an enhanced version of the one used in Ref. [6]. It has been extended to accommodate 5-species air ($N_2$, $O_2$, NO, N and O) and all relevant elastic,inelastic and reactive trajectory calculations involving these mixture components. The DMS calculation employed a 1D domain $10\,\mathrm{cm}$ in length sub-divided into $20\,000$ collision cells. The time step was kept constant at $\Delta t_{\mathrm{DMS}} = 0.5\,\mathrm{ns}$. For the classical trajectory calculations we employed the

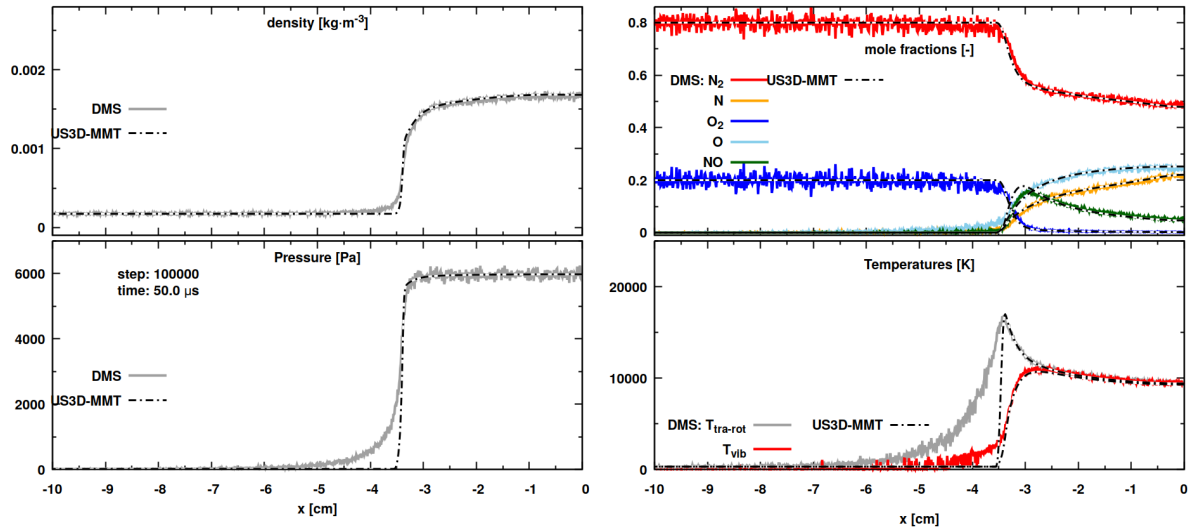


**Fig 1.** Normal shock in air after $50\,\mu$s: DMS (color lines) vs. CFD (dash-dotted black). Upper half: mixture density (left) and species mole fractions (right), lower half: static pressure (left) and gas trans-rotational and vibrational temperatures (right)

Velocity Verlet scheme with a time step of $\Delta t_{\text{CT}} = 0.05$ fs, a species-pair- and relative-collision-energy-dependent $b_{\text{max}}$ and a cut-off distance $D_c = 15$ Å between collision partners.

The corresponding CFD calculations with US3D as the solver are set up in an analogous manner. The computational domain consists of a single row of cells along the $x$-axis, with symmetry boundaries applied on all faces in the $y$- and $z$-planes. A supersonic inlet boundary condition is imposed at the leftmost $x-$face with the "upstream" flow properties from Table 1, but inflow speed $u_1' = 5588.2\,\text{m/s}$. On the opposite end of the domain, a symmetry boundary is applied as well. The finite-volume scheme employed relied on Modified Steger-Warming flux-vector splitting and 2nd order inviscid fluxes with a MUSCL extrapolation for primitive variables. Time-accurate integration was performed using a 3rd order Runge-Kutta scheme with a constant time step $\Delta t_{\text{CFD}} = 50$ ns. Dissipative transport fluxes of mass, momentum and energy are computed using the Self-Consistent Effective Binary Diffusion (SCEBD) model [11] with diffusion coefficients based on Gupta-Yos Collision integral data, viscosity derived from Gupta collision integrals [12] and thermal conductivity including internal degrees of freedom computed through the Eucken relation. The most up-to-date set of reactions accounted for in these simulations is listed in Table 2 of Ref. [10]. Note that all kinetic rate data employed in the CFD calculations were derived from QCT calculations employing the same ab initio PESs used in the 1D-benchmark DMS run. This includes all reaction rate coefficients and average vibrational energy removed by dissociation shown in Figs. 2 and 3 of Ref. [10]. Furthermore, all vibrational relaxation time constants in the current CFD calculations are calculated based on the curve fits shown in Fig. 1 of Ref. [10].

The CFD time step was kept at a constant multiple of $\Delta t_{\text{DMS}}$ so it would remain in sync with the DMS calculation and allow for direct comparison of both flow fields at specific times. Figure 1 shows such a comparison plot between the CFD solutions (black dash-dotted lines) vs. DMS (color lines) for the 5-species air mixture. In the upper row we plot mixture density (left) and mixture composition (right). The lower row shows static pressure (left) and temperature modes (right). This flow field represents a snapshot of the unsteady solution $50\,\mu$s after the simulation has started. The CFD model captures the post-shock flow field predicted by DMS with remarkable accuracy. The only major discrepancies are observed in the pressure and trans-rotational temperature profiles upstream of the shock front, which cannot be exactly resolved by Navier-Stokes-based flow solvers.

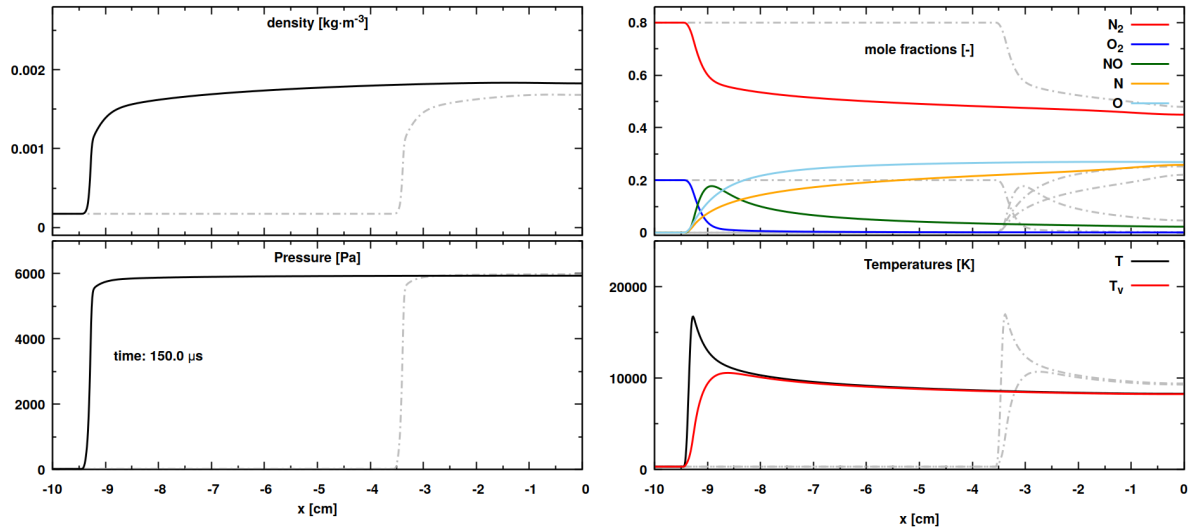


**Fig 2.** Normal shock in air after $150\,\mu$s: DMS (color lines) vs. CFD (dash-dotted black). Upper half: mixture density (left) and species mole fractions (right), lower half: static pressure (left) and gas trans-rotational and vibrational temperatures (right)

Note that in Fig. 1 the gas state near the symmetry boundary at $x = 0$ does not yet correspond to the "downstream" equilibrium conditions from Table 1. At this instant the shock has not traveled upstream far enough to reveal the complete thermo-chemical relaxation zone behind it. Indeed, simulating the post-shock region for full relaxation toward thermal and chemical equilibrium would require a domain length several orders of magnitude larger than the $10\,$cm being shown here. Such length and time scales are prohibitively large for the first-principles method and the solution after $50\,\mu$s represents the latest available DMS flow field snapshot. However, the CFD calculation can easily be continued for longer physical times. In Fig. 2 we plot the CFD flow field at time $150\,\mu$s (solid color lines). By this time the shock wave has almost reached the left domain boundary. For reference the dashed gray lines re-trace the CFD profiles at $50\,\mu$s from Fig. 1. After a total of $150\,\mu$s the post-shock flow field has evolved further and the gas state at the right boundary has moved somewhat closer to the expected post-shock equilibrium conditions from Table 1.

## 3. Nitrogen flow over blunt wedge

In this section we report on a two-dimensional hypersonic flow field involving the dissociation of nitrogen under thermo-chemical nonequilibrium conditions. This case was originally studied with the DMS method by Grover et al. [7] and thus provides another opportunity to compare CFD predictions involving the MMT dissociation model to benchmark solutions that themselves rely on nothing but the Minnesota ab initio PESs.

A diagram of the surface geometry is shown in Fig. 3 of Ref. [7]. From left to right it consists of a circular arc section of radius $r_l = 10\,$mm, which smoothly transitions into a straight section with wedge angle $\theta = 15°$. The overall distance from the forward stagnation point to the rear end of the wedge is $l = 40\,$mm. This also marks the location of the outflow boundary, where a supersonic outlet condition is imposed. Only the upper half of the wedge was simulated by Grover et al. and in our CFD calculations we follow the same approach by imposing a symmetry condition along the $x-$axis between the inflow boundary to the left and the wedge tip at $(x = 0, y = 0)$. All parameters needed to specify the uniform freestream are summarized in Table 2. The inflow boundary itself starts $20\,$mm upstream of the wedge tip. This is more than enough to accommodate the bow shock stand-off distance at steady state. From

there on, the inflow boundary curves around the wedge at a constant distance of $20$ mm. The wedge surface itself was treated as an isothermal wall boundary at temperature $T_w = 1\,000$ K.

The flow domain was discretized by a computational grid consisting of roughly $60\,000$ hexahedral cells (about $200$ in wall-normal direction $\times$ $300$ along the wedge surface). Nearly half the cells were allocated to cover the flow field above the leading edge, with the remaining half left to resolve flow over the straight portion further downstream. The US3D solver only operates on three-dimensional computational domains, which means that the two-dimensional geometry defined in the $(x, y)$-plane was extruded by one cell width along the perpendicular axis. Symmetry boundary conditions imposed on both resulting $z$-planes ensure that the computed flow field remains two-dimensional. The finite-volume scheme employed relied on Modified Steger-Warming flux-vector splitting and 2nd order inviscid fluxes with a MUSCL extrapolation for primitive variables. Starting from a flow field initialized to freestream quantities, implicit time integration via the data-parallel line relaxation (DPLR) scheme lead to the final steady-state solution.

With an estimated free-stream viscosity of $1.4 \times 10^{-5}$ Pa, velocity and density taken from Table 2 and the wedge radius as reference length, one arrives at an approximate freestream Reynolds number of $\mathrm{Re}_{\infty,r_l} \approx 8000$. This can be considered low enough for the flow to remain laminar throughout the entire domain and therefore no turbulence model was employed. Grid spacing toward the wall was gradually reduced to allow for adequate resolution of the viscous boundary layer, with a cell height at the surface equal to $0.001$ mm along the entire geometry. This allowed for comfortably satisfying the $y^+ < 1$ condition along the entire surface for the final flow field.

**Table 2.** Free stream conditions used for CFD simulation of wedge case. Freestream composition specified in terms of species mass fractions

| $u_\infty$ [m/s] | $\rho_\infty$ [g/m$^3$] | $T_\infty = T^{\mathrm{v}}_\infty$ [K] | $c_{\mathrm{N}_2,\infty}$ | $c_{\mathrm{N},\infty}$ |
|---|---|---|---|---|
| 6 500 | 1.8 | 226 | 1.0 | 0.0 |

When the free-stream mean free path is estimated with a hard-sphere diameter of $4$ Å, the corresponding Knudsen number based on wedge nose radius becomes $\mathrm{Kn}_{\infty,r_l} \approx 0.004$. Thus, from a global perspective the flow can be considered to be in the near-continuum regime where the Navier-Stokes equations are applicable. Nevertheless, locally it may exhibit regions of continuum breakdown, mainly surrounding the bow shock and within the boundary layer in immediate vicinity of the surface. Strictly speaking, this calls into question the use of the no-slip boundary condition and suggests that it be replaced by a finite-slip model. However, since the emphasis of the present calculations is on verification of the gas-phase chemistry and vibrational relaxation model against DMS, the gas-surface interaction was considered to be of secondary importance. Thus, it was assumed that zero velocity slip and no temperature jump occur at the wall. In future calculations this case will be re-examined with an appropriate slip boundary condition.

Just as in Sec. 2, in our CFD calculations the MMT chemistry model handles nonequilibrium dissociation of all diatomic species. Since in the present case the freestream consists only of molecular nitrogen, the only reactions of concern are the two dissociation reactions $2\mathrm{N}_2 \rightarrow 2\mathrm{N} + \mathrm{N}_2$ and $\mathrm{N}_2 + \mathrm{N} \rightarrow 3\mathrm{N}$. Note that the benchmark DMS calculations only accounted for the reactions in the forward sense, but neglected the possible recombination reactions. In our study we carried out separate CFD calculations with and without recombination enabled to assess their overall influence on the results.

As was the case in Sec. 2 the required characteristic vibration-translational relaxation times are computed based on a correlation fitted to DMS-derived data for $p\tau^{\mathrm{v-t}}_{\mathrm{N}_2-\mathrm{N}_2}(T)$, $p\tau^{\mathrm{v-t}}_{\mathrm{N}_2-\mathrm{N}}(T)$ computed with the Minnesota $\mathrm{N}_4$ and $\mathrm{N}_3$ ab initio PESs (see Figs.2(a) and 3(a) of Ref. [13]). For the present calculations diffusive transport of mass, momentum and energy is modeled via long-established models, already implemented in US3D. The viscosity of the $\mathrm{N}_2/\mathrm{N}$ mixture is computed using Blottner fits [14] and the Wilke mixing rule [15]. The thermal conductivity is derived from viscosity via the Eucken relation, while mass diffusion fluxes are computed with Fick's law and diffusion coefficients based on a constant Lewis number.

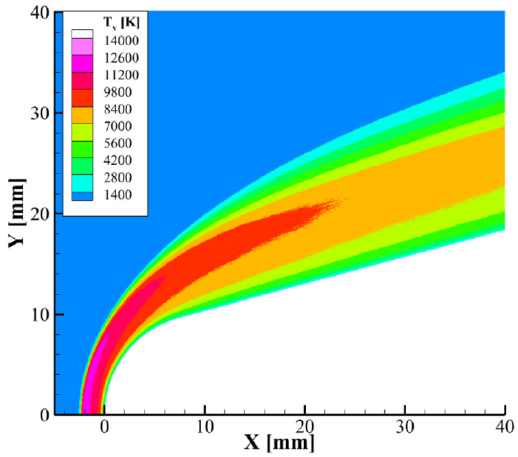


**(a)** DMS (Fig.5(c) of Ref. [7])

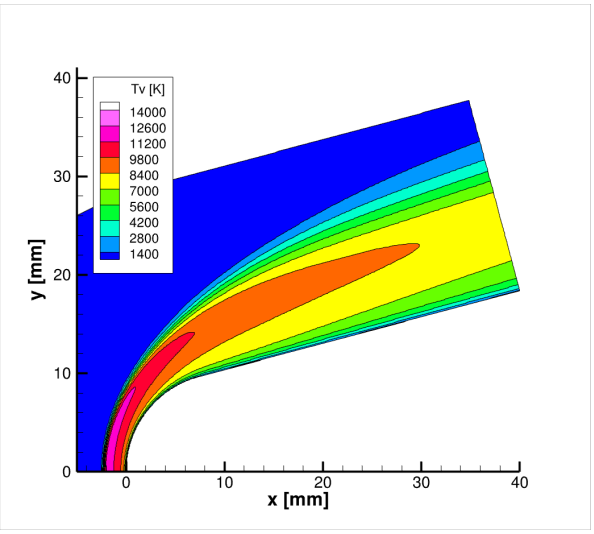


**(b)** CFD-MMT (colors: no recomb., lines: with recomb.)

**Fig 3.** Blunt wedge: vibrational temperature

We now compare the steady-state flow field resulting from our CFD calculation with that of the DMS benchmark solution. First, Fig. 3 shows vibrational temperature contours, with the DMS flow field on the left and our CFD result on the right. In the CFD plot, contour colors represent the result without recombination, while the black lines show the corresponding flow field with recombination included. The DMS plot has been lifted directly from Fig. 5(c) of Ref. [7] and contour levels on the CFD plot have been set accordingly. Although the levels are identical, note that color-coding of both plots is slightly different. Nevertheless, the two plots allow us to compare the degree of vibrational excitation across the flow field predicted by both methods. As is to be expected, the highest vibrational temperatures are reached downstream of the bow shock, along the stagnation streamline ($y = 0$). At this location the bow shock sits normal to the incoming freestream and causes its strongest deceleration, which forces the flow to become subsonic. Both methods predict similar peak vibrational temperatures (in the range $11\,200\,\text{K} < T_v < 12\,600\,\text{K}$) roughly $1.2 - 2.2\,\text{mm}$ upstream of the stagnation point. As the flow expands around the leading edge the vibrational temperature gradually decreases. This process takes place at a slightly quicker pace in the DMS flow field. For instance, the edge of contour $8\,400 < T_v < 9\,800$ (red in Fig. 3a) extends to an maximum $x-$location roughly between $21$ and $22\,\text{mm}$. By contrast, the same interval in the CFD-MMT solution (dark orange in in Fig. 3b) reaches further downstream, up to $x \approx 28\,\text{mm}$.

Next, in Fig. 4 we compare the amount of atomic nitrogen present in the flow as predicted by our CFD calculation (right) to the benchmark DMS results (left) of Grover et al. (taken from Fig. 6 of Ref. [7]). As for the previous figure, for easier comparison our CFD-MMT flow field is plotted using the same contour levels as the DMS solution. Both methods predict noticeable levels of nitrogen dissociation behind the bow shock. In the DMS flow field of Fig. 4a, $c_\text{N}$-values surpass 20% within the layer immediately $1\,\text{mm}$ adjacent to the surface (purple contour). This high-concentration region extends along the rounded leading edge and partially into the straight portion. However, as one moves further downstream the near-wall atomic nitrogen mass fraction decreases gradually to values below 17.5% (orange contour). Recall that the benchmark DMS calculations did not model recombination reactions, which means that the drop in $c_\text{N}$ cannot be caused by chemical effects. Instead, Grover et al. [7] attributed it to temperature-gradient driven mass diffusion (Soret effect), which acts to concentrate the heavier species ($N_2$) near the relatively cold wall.

Now contrast this behavior with the CFD-MMT flow field shown in Fig. 4b. Although our CFD calculation predicts similar peak $c_\text{N}$-values to DMS in the near-wall region surrounding the leading edge, it does

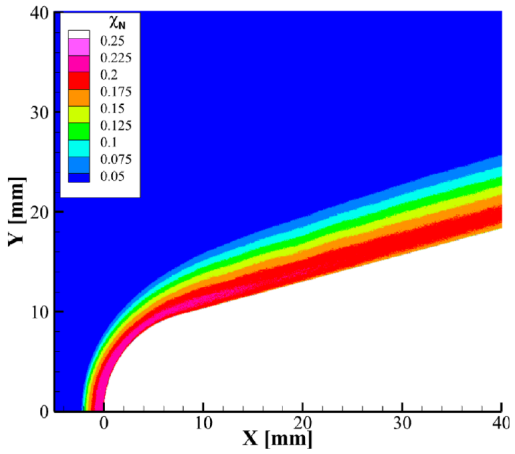


**(a)** DMS (Fig. 6 of Ref. [7])

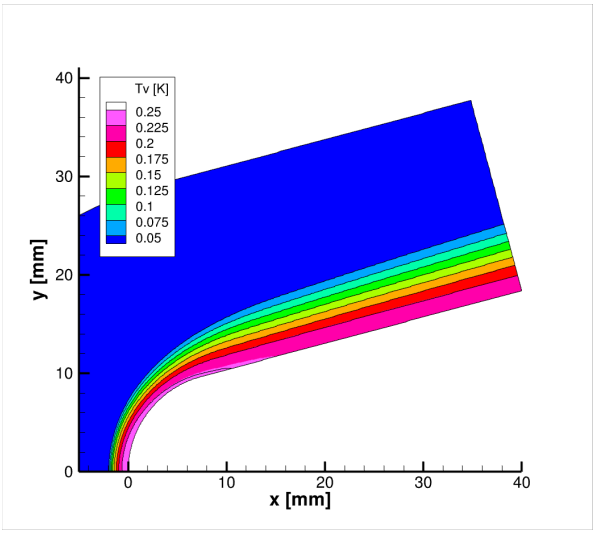


**(b)** CFD-MMT (colors: no recomb., lines: with recomb.)

**Fig 4.** Blunt wedge: atomic nitrogen mass fraction

not show the same decrease in atomic nitrogen mass fraction as DMS further downstream. Indeed, in the CFD solution the atomic nitrogen mass fraction in wall vicinity remains steadily above 20% across the entire domain. However, note that the vibrational temperatures in wall vicinity along the straight wedge section are too low to trigger nitrogen dissociation. Just as in the DMS benchmark, in our CFD calculation all of the atomic nitrogen present in the flow is produced within the narrow region along the stagnation streamline and the rounded leading edge. From there on, it is transported across the flow field, primarily by advection and, to a lesser degree, by diffusion. Thus, chemical reaction effects cannot explain this discrepancy. Instead, recall that in our current CFD calculations mass diffusion is described by Fick's law alone. This means that the only driving forces taken into account when calculating the diffusion fluxes are those due to species mass-fraction gradients. Since this means that thermal diffusion is explicitly ignored in our CFD calculations, the near-wall differences with respect to the DMS flow field are not surprising.

The preceding reasoning can be supported by examining wall-normal flow field profiles extracted at specific locations along the body. First, in Fig. 5 we focus on the stagnation streamline. The left figure shows temperatures and the one on the right the corresponding atomic nitrogen mass fraction along the stagnation streamline. The DMS benchmark solution is plotted in gray and the two CFD results with the MMT model is shown in red. Solid lines represent the result without, whereas dotted lines the one with recombination included. A third set of blue curves represents separate CFD calculations employing the standard Park two-temperature model for nitrogen dissociation, along with Park's recommended rate coefficients [16], plus vibrational relaxation rates based on the Millikan-White correlation together with the high-temperature correction from Ref. [16]. These results represent the current state-of-the-art multi-temperature nonequilibrium chemistry model. Note that these Park-model CFD calculations were also carried out with (dotted blue) and without recombination reactions (solid blue).

In Fig. 5a for each of the three solutions we plot a combined translation-rotational temperature $T_{\mathrm{t-r}}$ together with the corresponding vibrational temperature $T_{\mathrm{v}}$. Note that when Grover et al. originally presented their DMS results for this wedge geometry [7], they reported separate translational and rotational temperatures for $N_2$. This was the most straightforward approach, since in these first-principles calculations the two modes may evolve independently. By contrast, in our two-temperature CFD nonequilibrium modeling (either using MMT or the Park model) the rotational and translational modes of the gas are, by construction, assumed to be equilibrated at a common temperature. Thus, we only have access a combined translation-rotational temperature of the mixture. In order to make the comparison between the

DMS and multi-temperature CFD results more meaningful, we chose to post-process the original DMS flow field data (provided to the authors courtesy of Grover et al.) and compute an equivalent translation-rotational temperature: $T_{\mathrm{t-r,mix}} = \frac{3}{5}T_{\mathrm{tra,mix}} + \frac{2}{5}T_{\mathrm{rot,N_2}}$. The DMS mixture translational temperature in turn was computed as the mole-fraction-weighted average $T_{\mathrm{tra,mix}} = x_{\mathrm{N_2}}T_{\mathrm{tra,N_2}} + x_{\mathrm{N}}T_{\mathrm{tra,N}}$.

A few things stand out when comparing flow properties along the stagnation line. First, the DMS-derived solution exhibits the largest shock stand-off distance of all three, but is closely followed by the CFD-MMT solution. Indeed, the DMS and CFD-MMT temperature profiles share several similarities. For both solutions the peak of $T_{\mathrm{t-r}}$ lies at roughly $18\,000$ K, with the CFD-MMT solution lagging behind DMS only by about $0.3$ mm. Similar behavior can be observed for $T_{\mathrm{v}}$, whose peak is predicted by DMS and CFD-MMT to lie around $12\,000$ K. The $T_{\mathrm{t-r}}$-peak predicted with the Park model is closer to $16\,000$ K and lies noticeably closer to the body than for both preceding solutions. Although the peak vibrational temperature predicted with the Park model is roughly the same as that for DMS and CFD-MMT, the Park $T_{\mathrm{v}}$-profile overshoots the corresponding $T_{\mathrm{t-r}}$ curve roughly $1.7$ mm from the wall. From there on until the stagnation point the vibrational temperature remains noticeably higher than the translational one. Neither the DMS, nor the CFD-MMT solutions exhibit this type of temperature inversion along the stagnation streamline. In close proximity of the stagnation point the temperature profiles for both CFD solutions become almost identical to each other, but both also deviate from the DMS profile to a similar degree. The benchmark temperature profile exhibits a noticeably weaker wall-normal temperature gradient than the CFD solutions. Notice that the presence, or absence of recombination reactions has an almost negligible effect on either of the CFD temperature profiles along the stagnation streamline.

In Fig. 5b we plot the corresponding atomic nitrogen mass fraction profiles for the three solutions. The DMS benchmark profile (gray line) for $c_{\mathrm{N}}$ begins to increase along the stagnation streamline slightly ahead of both the CFD-MMT (red) and CFD-Park (blue) solutions. The DMS peak is reached roughly $0.5$ mm from the wall, before a small dip at the stagnation point itself. The CFD-MMT solution initially lags behind the DMS profile, but surpasses it roughly $1$ mm from the wall. From there on it continues to rise until reaching a plateau of $c_{\mathrm{N}} \approx 0.24$ just ahead of the stagnation point. Notice that when recombination is taken into account (dotted red line) a small, barely noticeably dip in the atomic nitrogen mass fraction appears roughly $0.5$ mm from the wall. The corresponding behavior for the Park solution is qualitatively similar to the CFD-MMT profile, but more pronounced. Consistent with the observed temperature behavior, the atomic nitrogen mass fraction with the Park model lags behind both the DMS and MMT curves. However, the Park model predicts noticeably faster dissociation than both other solutions and quickly surpasses both of them half-way along the stagnation streamline. When recombination is neglected (solid blue line), the Park solution reaches a maximum value of $c_{\mathrm{N}} \approx 0.27$ at the wall. However, when it is taken into account (dotted blue line), a noticeable drop in $c_{\mathrm{N}}$ is observed toward the stagnation point. Keep in mind that, unlike DMS, neither of the CFD solutions account for thermal diffusion near the wall. Thus, any dip in atomic nitrogen near the wall can only be attributed to recombination. By contrast, when recombination is neglected, both CFD mass fraction profiles exhibit zero wall-normal mass-fraction gradients.

A similar analysis as for the stagnation streamline can be performed for wall-normal profiles at several stations downstream. In Fig. 6 and 7 we summarize such plots for the two locations marking the beginning (at $x = 10$ mm) and end (at $x = 40$ mm) of the straight portion of the wedge. Figures 6a and 6b show the wall-normal temperature and atomic nitrogen mass fraction for $x = 10$ mm respectively, whereas Figs. 7a and 7b show the same information for the $x = 40$ mm station. All line colors and patterns are identical to those defined in Fig. 5 with the only difference that in Figs. 6 and 7 the wall-normal direction is now plotted along the ordinate axis and the temperatures/atomic nitrogen concentration along the abscissa.

One major difference to observe when comparing the temperature profiles to those along the stagnation streamline is that in Figs. 6a and 7a all three solution types exhibit noticeable $T_{\mathrm{v}}$-overshoots with respect to their corresponding $T_{\mathrm{t-r}}$ wall-normal profiles. For the $x = 10$ mm-location this occurs roughly $6$ mm from the surface and for the $x = 40$ mm-station it happens at a wall-normal distance of roughly $11 - 12$ mm. Notice that, opposite to the stagnation streamline, at both these downstream locations the main

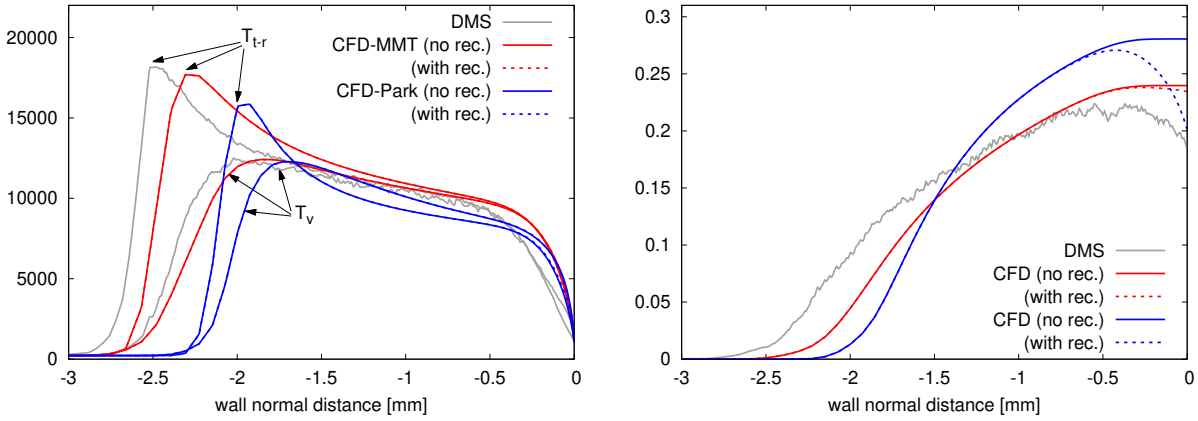


**(a)** Temperatures [K] **(b)** atomic nitrogen mass fraction

**Fig 5.** Blunt wedge: comparison of wall normal profiles on stagnation streamline for DMS benchmark solution (gray), CFD with MMT model (red) and with Park model (blue). Gas-phase recombination in CFD solution neglected (solid lines) vs. included (dotted lines)

flow direction is nearly perpendicular to the wall-normal. Thus, the massive $T_\mathrm{v}$-overshoots observed at these locations cannot be attributed to shock-heating of gas propagating along the wall-normals. Instead, they are primarily a consequence of vibrationally excited gas being advected from the region surrounding the stagnation streamline, which has not had enough time to relax toward equilibrium when passing the two sampling stations.

The main point to be made by the four plots in Figs. 6 and 7 is that the CFD-MMT profiles generally are in much closer agreement whit the DMS benchmark than the CFD-Park curves. At both $x-$locations the Park model predicts a noticeably steeper rise in atomic nitrogen concentration toward the surface than MMT, or DMS. Furthermore, when recombination is accounted for with the Park model (dotted vs. solid blue lines) it again has a much stronger effect in reducing $c_\mathrm{N}$ near the wall than is seen for the MMT model (dotted vs. solid red). As noted before, this recombination effect in the CFD-Park result is not present in the DMS reference profiles. For those profiles the decrease in $c_\mathrm{N}$ near the wall is attributed exclusively to thermal diffusion.

## 4. Oxygen flow over double-cone geometry

In one of their most recent large-scale DMS calculations Grover et al. [8] simulated hypersonic flow of partially dissociated oxygen over a double-cone geometry. This geometry corresponds to a test article originally studied in the Large Energy National Shock (LENS) facility at the Calspan - University of Buffalo Research Center (CUBRC). This test case was originally simulated with CFD as "run 88" by Nompelis and Candler [17], using a predecessor to the US3D code employed in our own current comparison calculations. Note that in their DMS benchmark calculations Grover et al. [8] made slight modifications to the original free stream conditions listed for CUBRC "run 88". These updated conditions are summarized in Table 3.

**Table 3.** Free stream and boundary conditions used for CFD simulation of double cone case. Freestream composition specified in terms of species mass fractions

| $u_\infty$ [m/s] | $\rho_\infty$ [g/m$^3$] | $T_\infty = T^\mathrm{v}_\infty$ [K] | $c_{\mathrm{O}_2,\infty}$ | $c_{\mathrm{O},\infty}$ |
|---|---|---|---|---|
| 3853 | 1.0613 | 606 | 0.9744 | 0.0256 |

In our current calculations a no-slip, isothermal wall boundary condition with constant wall temperature $T_w = 300\,\mathrm{K}$ was imposed along the entire double-cone surface. A diagram of the test article geometry

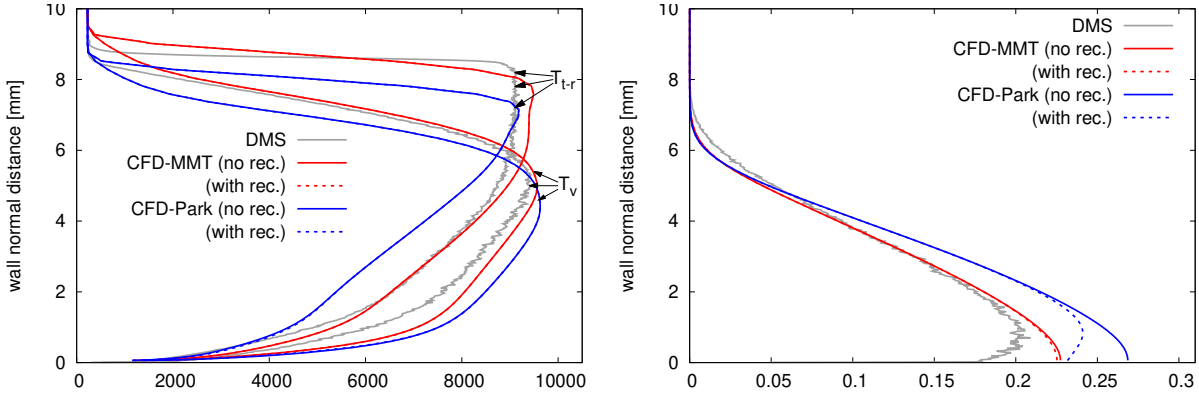


**(a)** Temperatures [K] at $x = 10\,\text{mm}$ **(b)** atomic nitrogen mass fraction at $x = 10\,\text{mm}$

**Fig 6.** Blunt wedge: comparison of wall normal profiles at beginning of straight wedge section for DMS benchmark solution (gray), CFD with MMT model (red) and with Park model (blue). Gas-phase recombination in CFD solution neglected (solid lines) vs. included (dotted lines)

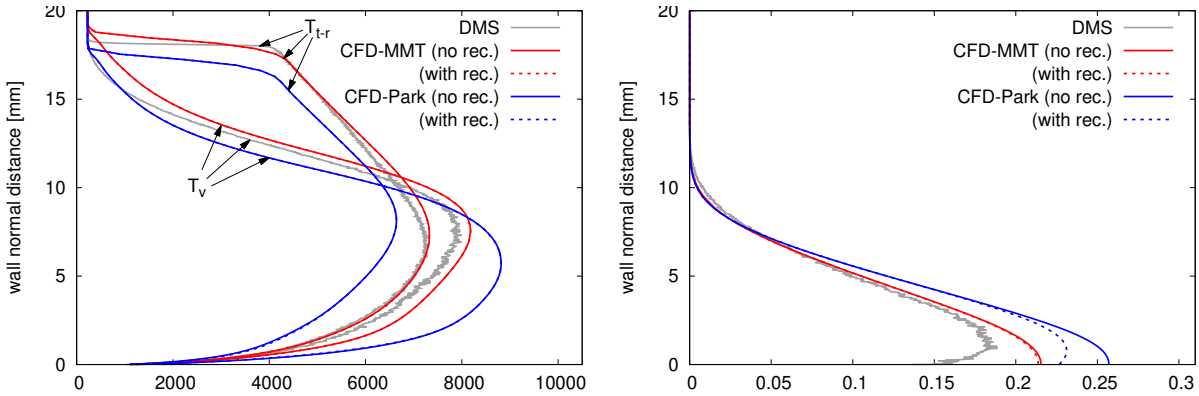


**(a)** Temperatures [K] at $x = 40\,\text{mm}$ **(b)** atomic nitrogen mass fraction at $x = 40\,\text{mm}$

**Fig 7.** Blunt wedge: comparison of wall normal profiles at end of straight wedge section for DMS benchmark solution (gray), CFD with MMT model (red) and with Park model (blue). Gas-phase recombination in CFD solution neglected (solid lines) vs. included (dotted lines)

is shown in Fig. 1(c) of Grover et al. [8]. The incoming freestream is assumed to be perfectly uniform and aligned with the central axis of the double-cone geometry. This makes it possible to simulate the flow as axially symmetric. Within US3D such simulations are carried out on a three-dimensional grid in regular Cartesian coordinates, which represents a "pie-slice" of single-cell width in the azimuthal direction. Symmetry boundary conditions are imposed on both azimuthal planes to mimic axisymmetric behavior. This approximation is valid as long as the slice angle is kept small. In our CFD calculations we rely on body-fitted hexahedral grids generated using the same method as those used originally by Nompelis and Candler [17]. Different grids, each with roughly double their predecessor's cell count in the shock layer were tested. Grid convergence was achieved with a spacing of roughly $2\,000$ nodes along the double-cone surface by $1\,000$ in the perpendicular, wall-normal direction. Grid spacing toward the wall was gradually reduced so as to adequately resolve the boundary layer.

The exact same spatial discretization and time integration schemes as for the blunt wedge case of Sec. 3 were employed. It is worth mentioning that prior studies [18] have shown flow over this double-cone geometry not always reaching steady state given certain inflow conditions. Fortunately, for the particular freestream and boundary conditions imposed in our present case a time-invariant steady-state flow field is eventually established. This was confirmed by monitoring the evolution of flow-field and surface distributions over roughly 50 flow-through times, starting out from a flow field initialized to the freestream conditions.

Just as in Secs. 2 and 3, we rely on the MMT chemistry model to model nonequilibrium dissociation reactions. For this case the only relevant reactions are $2\mathrm{O}_2 \rightarrow 2\mathrm{O}+\mathrm{O}_2$ and $\mathrm{O}_2+\mathrm{O} \rightarrow 3\mathrm{O}$. Note again that the benchmark DMS calculations only accounted for the reactions in the forward sense, but neglected the possible recombination reactions. In our present study we focus on the CFD calculations without recombination enabled. The necessary characteristic vibration-translational relaxation times are again computed based on a correlation fitted to DMS-derived data for $p\tau^{\mathrm{V-t}}_{\mathrm{O_2-O_2}}(T)$, $p\tau^{\mathrm{V-t}}_{\mathrm{O_2-O}}(T)$ computed with the Minnesota $\mathrm{O}_4$ and $\mathrm{O}_3$ ab initio PESs (see Figs.2(a) and 3(b) of Ref. [13]). Dissipative transport fluxes of mass, momentum and energy are computed using the Self-Consistent Effective Binary Diffusion (SCEBD) model [11] with diffusion coefficients based on Gupta-Yos Collision integral data, viscosity derived from Gupta collision integrals [12] and thermal conductivity including internal degrees of freedom computed through the Eucken relation.

In Fig. 8 we show a close-up of the flow field surrounding the junction between both cones. The density contours as predicted by the DMS calculations of Grover et al. (taken from Fig. 3(a) of Ref. [8]) are shown on the left, in Fig. 8a. The sonic line is shown in black, along with multiple flow features produced by the interaction of both oblique bow shocks and a boundary layer separation region at the cone junction. Some remaining statistical noise inherent to the DMS solution is evident by the irregular shape of the sonic line surrounding the subsonic pocket just above a triple point. Meanwhile, Fig. 8b shows our corresponding results obtained with US3D together with the MMT chemistry model. Contour levels and color palette were chosen to match those of Fig. 8a. At first glance both flow fields are in close agreement regarding the presence and general location of all relevant flow features. However, their precise location does differ slightly. For instance, in the DMS solution the boundary layer separation point on the first cone lies at $x \approx 7.6\,\mathrm{cm}$, whereas in the CFD-MMT solution it appears slightly further downstream, at $x \approx 7.7\,\mathrm{cm}$. Also, the triple point location differs slightly between both solutions. For the DMS it is located at $(x, y) \approx (9.76\,\mathrm{cm}, 5.63\,\mathrm{cm})$, whereas in the CFD-MMT solution the triple point lies at $(x, y) = (9.58\,\mathrm{cm}, 5.48\,\mathrm{cm})$.

Figure 9 compares the corresponding atomic oxygen concentration distribution predicted by the DMS benchmark (left) to our CFD result with the MMT model (right). The DMS flow field plot in Fig. 9a was taken directly from Fig. 2(b) of Grover et al. [8]. Both methods predict similar distributions of atomic oxygen across the flow field and that practically all of the dissociation is concentrated in the subsonic pocket located ahead of the second cone. Note that just above the triple point the incoming freestream traverses a nearly normal bow shock. Thus, the post-shock gas is decelerated to subsonic speeds and strongly compressed within a short distance. This compression heating is what ultimately causes the added oxygen dissociation. From there on the flow turns upward by a sharp angle and with it the newly

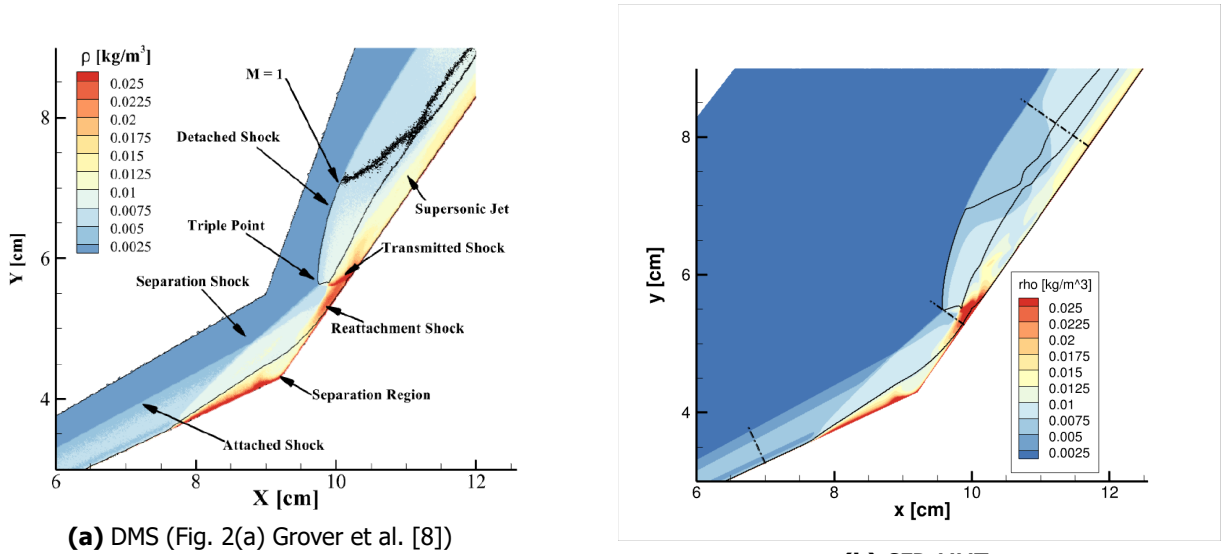


**(a)** DMS (Fig. 2(a) Grover et al. [8])

**(b)** CFD-MMT

**Fig 8.** Double cone: density contours at cone junction

formed atomic oxygen is advected downstream, roughly parallel to the second cone's surface. Both the DMS and CFD-MMT solutions predict a supersonic jet shielding this subsonic region with high atomic oxygen concentration from the actual wall.

The contour plots in Figs. 8 and 9 give a general overview of all flow features, but make precise comparisons between both results difficult. We therefore extract wall-normal profiles at two selected sampling stations. The first is located on the $25$-degree cone, emanating from the surface at $x = 7\,\text{cm}$. The second wall-normal profile is extracted on the $55$-degree cone, starting at $x = 11.7\,\text{cm}$. Focusing on the $7\,\text{cm}$-location first, in Fig. 10a we compare DMS-derived temperature profiles taken from Fig. 3(a) of Grover et al. [8] to our CFD-MMT predictions. The solid blue, black and red lines represent translational, rotational and vibrational temperatures respectively, extracted from the DMS calculations. Our CFD-MMT profile for the combined translation-rotational temperature is shown in yellow, whereas the vibrational temperature is plotted in green. Judging by the departure between $T_\text{t}$ and $T_\text{r}$ profiles of Grover et al. the region of rotational nonequilibrium is fairly narrow. Thus, we can reasonably compare them to our CFD-derived $T_\text{t-r}$ profile. We see both methods predicting nearly identical shock stand-off distances. The CFD-MMT trans-rotational temperature (yellow) in the shock layer closely follows the DMS profiles (black and blue), but is offset to roughly $100 - 150\,\text{K}$ higher values. At the same time both methods predict nearly identical $T_\text{v}$-profiles. The corresponding wall-normal atomic oxygen mass fraction profiles are shown in Fig. 10b. The DMS-derived profile (taken from Fig. 3(b) of Grover et al. [8]) is plotted as the solid green line, while our CFD-MMT profile is represented by a solid black line. Note that the DMS profile is affected by significant statistical noise, but averages out to a near-constant value roughly corresponding to the freestream $c_\text{O}$ listed in Table 3. Our CFD-MMT profile shows similar behavior, with no concentration gradients along the wall-normal. Clearly, the temperature rise across the oblique shock ahead of the 25-degree cone is not strong enough to trigger oxygen dissociation.

The picture is somewhat different at the second sampling location further downstream. In Fig. 11a we compare wall-normal temperatures at the $x = 11.7\,\text{cm}$ location. The DMS profiles were taken from Fig. 3(e) of Grover et al. [8] and all line color and labeling conventions are carried over from Fig. 10a. The more severe flow deflection due to the 55-degree cone now causes post-shock temperatures to rise above $5\,000\,\text{K}$, which is enough to trigger noticeable amounts of oxygen dissociation. Agreement between the DMS and CFD temperature profiles is good, but not perfect. Judging from the DMS-derived $T_\text{t}$ and $T_\text{r}$ profiles (black and blue lines) and the CFD-derived $T_\text{t-r}$ curve (yellow line), both methods predict a bow shock location at approximately $1.1\,\text{cm}$ from the body surface. However, agreement

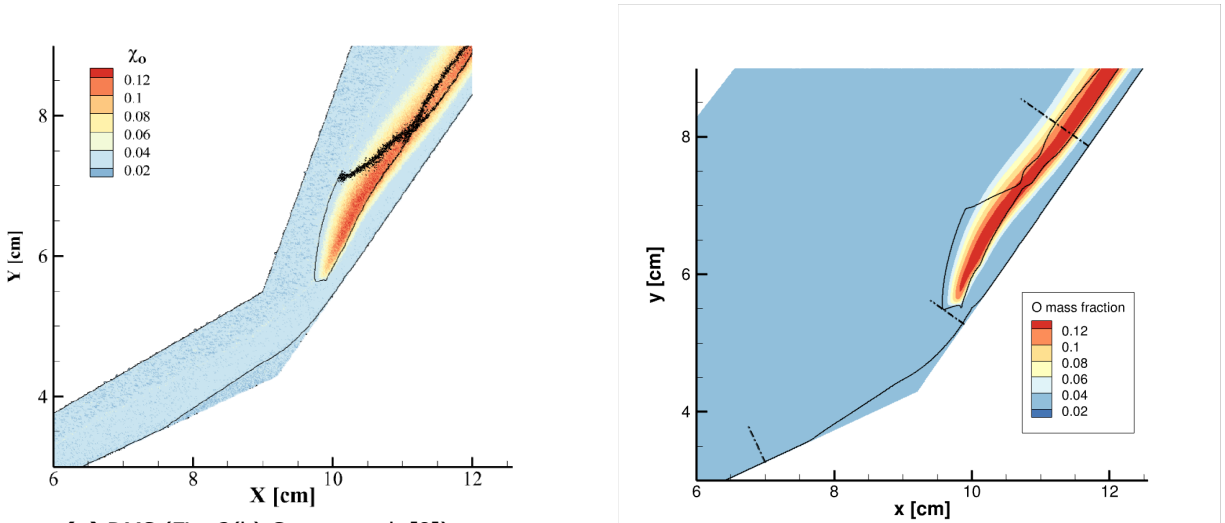


**(a)** DMS (Fig. 2(b) Grover et al. [8])

**(b)** CFD-MMT

**Fig 9.** Double cone: atomic oxygen mass fraction contours at cone junction

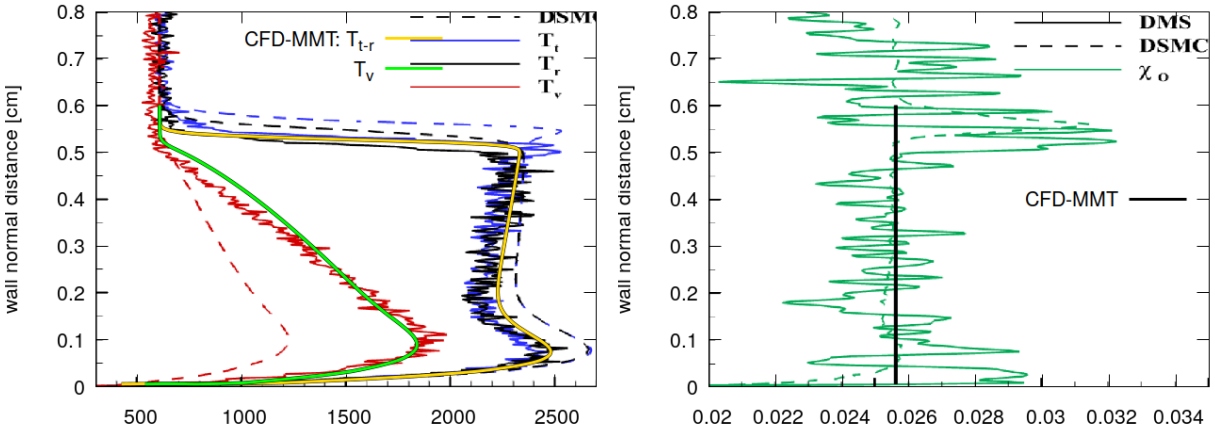


**(a)** Temperatures [K]

**(b)** O mass fraction

**Fig 10.** Double cone: comparison CFD-MMT vs. DMS for wall normal at $x = 7$ cm (DMS profiles from Figs. 3(a) and (b) of Grover et al. [8])

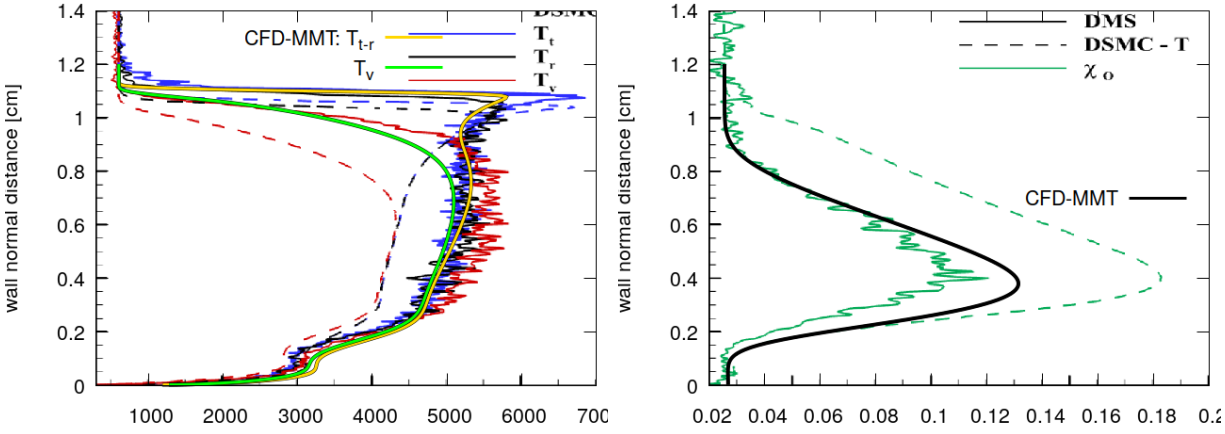


**(a)** Temperatures [K] **(b)** O mass fraction

**Fig 11.** Double cone: comparison CFD-MMT vs. DMS for wall normal at $x = 11.7$ cm (DMS profiles from Figs. 3(e) and (f) of Grover et al. [8])

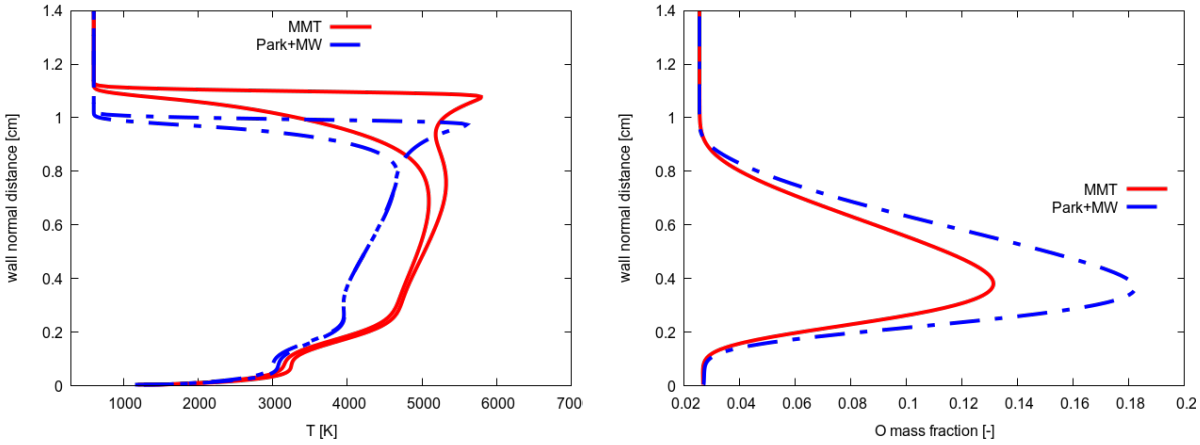


**(a)** Temperatures **(b)** O mass fraction

**Fig 12.** Double cone: comparison CFD-MMT vs. CFD-Park for wall normal at $x = 11.7$ cm

between the two methods' vibrational temperature profiles is not as close. The DMS-derived $T_\mathrm{v}$ (red line) shows an overshoot of up to $500$ K relative to the corresponding $T_\mathrm{t}$ and $T_\mathrm{r}$ profiles (black and blue lines) in the post-shock region, roughly $0.6 - 0.9$ cm from the wall. This overshoot is absent from our CFD predictions (green line), where the vibrational temperature remains slightly below its corresponding trans-rotational temperature (yellow line) along the entire extent of the wall-normal profile. On the other hand, both methods capture a small bump in temperature profiles nearly $0.1$ cm from the wall. This corresponds to the location of the aforementioned supersonic jet, layered between the subsonic pocket where the atomic oxygen concentration peaks and the wall. These $c_\mathrm{O}$-profiles are compared in Fig. 11b. The DMS solution is plotted as a solid green line and the CFD-MMT solution in black. Both methods predict a local maximum in the $c_\mathrm{O}$-profile roughly $0.35$ cm from the wall. The CFD-MMT-predicted peak lies roughly 20-30% above the DMS result, which may seem like a big deviation. However, when one contrasts CFD predictions obtained with the MMT model to those with the standard Park model (see Figs. 12a and 12b, it becomes clear that the MMT model does a much better job at matching the DMS benchmark solution.

## 5. Summary and future work

In this work we have used the US3D CFD code to perform verification studies on three distinct flow fields for the recently proposed Modified Marrone-Treanor multi-temperature nonequilibrium chemistry model for high-temperature air. Three available reference solutions generated via first-principles Direct Molecular Simulations allowed us to test the model in scenarios applicable to hypersonic flight and ground test facilities. The CFD results employing the MMT model show much closer agreement with the benchmark solutions than when state-of-the-art Park rates are used.

In addition to the appropriate nonequilibrium chemistry model, accurately reproducing these flow fields in CFD requires a treatment of dissipative transport (viscosity, thermal conductivity and mass diffusion coefficients) that is consistent with the first-principles benchmark method. The blunt wedge results of Sec. 3 in particular have revealed the need for including thermal diffusion (Soret and Dufour effects) to improve CFD transport modeling. As part of ongoing work we plan to implement DMS-consistent transport properties [19, 20] in US3D and carry out further comparison calculations.

## References

[1] J.D. Bender, P. Valentini, I. Nompelis, Y. Paukku, Z. Varga, D.G. Truhlar, T.E. Schwartzentruber, and G.V. Candler. An improved potential energy surface and multi-temperature quasiclassical trajectory calculations of $N_2 + N_2$ dissociation reactions. *The Journal of Chemical Physics*, 143:054304, 2015.

[2] R.S. Chaudhry, I.D. Boyd, E. Torres, T.E. Schwartzentruber, and G.V. Candler. Implementation of a Chemical Kinetics Model for Hypersonic Flows in Air for High-Performance CFD. In *AIAA Scitech 2020 Forum*, 2020. AIAA 2020-2191.

[3] G.V. Candler, H.B. Johnson, I. Nompelis, P.K. Subbareddy, T.W. Drayna, and V. Gidzak. Development of the US3D Code for Advanced Compressible and Reacting Flow Simulations. In *53rd AIAA Aerospace Sciences Meeting, Kissimmee, Florida*, 2015. AIAA 2015-1893.

[4] Erik Torres, Eric C. Geistfeld, and Thomas E. Schwartzentruber. High-temperature nonequilibrium air chemistry from first principles. *Journal of Thermophysics and Heat Transfer*, 2024. article in advance.

[5] T.E. Schwartzentruber, M.S. Grover, and P. Valentini. Direct Molecular Simulation of Nonequilibrium Dilute Gases. *Journal of Thermophysics and Heat Transfer*, 32(4):892–903, 2018.

[6] E. Torres and T.E. Schwartzentruber. Direct molecular simulation of oxygen dissociation across normal shocks. *Theoretical and Computational Fluid Dynamics*, 36(1):41–80, 2022.

[7] Maninder S. Grover, Ashley M. Verhoff, Paolo Valentini, and Nicholas J. Bisek. First principles simulation of reacting hypersonic flow over a blunt wedge. *Physics of Fluids*, 35(8):086106, 08 2023.

[8] Maninder S. Grover, Paolo Valentini, Nicholas J. Bisek, and Ashley M. Verhoff. *First principle simulation of CUBRC double cone experiments*. 2023.

[9] E. Torres, T. Gross, E. Geistfeld, and T.E. Schwartzentruber. Verification of nonequilibrium thermochemistry models for hypersonic cfd by first-principles simulation. In *Eleventh International Conference on Computational Fluid Dynamics (ICCFD11)*, 2022. ICCFD11-2022-2201.

[10] Erik Torres, Thomas Gross, and Thomas E. Schwartzentruber. Implementation of new multi-temperature nonequilibrium air chemistry model for cfd based on first-principles calculations. In *AIAA AVIATION 2023 Forum*, 2023. AIAA 2023-3489.

[11] J.D. Ramshaw. Self-Consistent Effective Binary Diffusion in Multicomponent Gas Mixtures. *Journal of Non-Equilibrium Thermodynamics*, 15(3):295–300, 1990.

[12] R.N. Gupta, J.M. Yos, R.A. Thompson, and K.P. Lee. A Review of Reaction Rates and Thermodynamic and Transport Properties for an 11-Species Air Model for Chemical and Thermal Nonequilibrium Calculations to 30 000 K. Technical report, NASA Langley Research Center, 1990. NASA Reference Publication 1232.

[13] E. Torres, E.C. Geistfeld, and T.E. Schwartzentruber. Direct molecular simulation of rovibrational relaxation and chemical reactions in air mixtures. In *AIAA SCITECH 2022 Forum*, 2022.

[14] F.G. Blottner, M. Johnson, and M. Ellis. Chemically Reacting Viscous Flow Program for Multi-Component Gas Mixtures. Technical report, Sandia Laboratories, Albuquerque, NM, 1971. SC-RR-70-754.

[15] C.R. Wilke. A Viscosity Equation for Gas Mixtures. *The Journal of Chemical Physics*, 18(4):517–519, 1950.

[16] C Park. Review of Chemical-Kinetic Problems of Future NASA Missions, I: Earth Entries. *Journal of Thermophysics and Heat Transfer*, 7(3):385–398, 1993.

[17] Ioannis Nompelis and Graham Candler. Numerical investigation of double-cone flow experiments with high-enthalpy effects. In *48th AIAA Aerospace Sciences Meeting Including the New Horizons Forum and Aerospace Exposition*, 2010. AIAA 2010-1283.

[18] Ioannis Nompelis and Graham V Candler. Numerical investigation of double-cone flows with high enthalpy effects. In *6th European Symposium on Aerothermodynamics for Space Vehicles*, volume 659, page 96, 2009.

[19] Paolo Valentini, Ashley M Verhoff, Maninder S Grover, and Nicholas J Bisek. First-principles predictions for shear viscosity of air components at high temperature. *Physical Chemistry Chemical Physics*, 25(13):9131–9139, 2023.

[20] Paolo Valentini, Maninder S. Grover, Nicholas J. Bisek, and Ashley M. Verhoff. Ab initio calculation of thermal conductivity: Application to molecular nitrogen. *Phys. Rev. Fluids*, 7:L071401, Jul 2022.